Supporting Information

Stable Oxygen Vacancies Engineered via Microenvironment-Regulated Diglyceryl Ether Decomposition for Solar-Driven Clean Water Generation

Chao Wang,[a,b] José M. Fraile,[b] Weian Wang,[c] Leichen Wang,[a] Baowei Shen,[a] Wei Ji,[a] Su Jing,*[a] Elísabet Pires, *[b] Jian Qu,[d] Chang Liu,[e] José A. Mayoral,[b] Wenzhong Yang[a]

[a] School of Chemistry and Molecular Engineering, Nanjing Tech University, Nanjing 211816, China.

[b] Instituto de Síntesis Química y Catálisis Homogénea, CSIC-Universidad de Zaragoza, Pedro Cerbuna 12, E-50009 Zaragoza, Spain.

[c] School of Chemistry and Chemical Engineering, Southeast University, Nanjing 210096, China.

[d] School of Materials Science and Engineering, Yancheng Institute of Technology, Yancheng 224051, China

[e] State Key Laboratory of Materials-Oriented Chemical Engineering, College of Chemical Engineering, Nanjing Tech University, Nanjing 211816, China

1. Calculation of the Evaporation Rate and Evaporation Efficiency[1, 2]

The evaporation rate ($\dot{m}$) of the samples was calculated by the following Equation 1:

$$\dot{m} = dm / (A\ dt) \quad (1)$$

Where m is the mass change of the entire evaporator, A is the irradiated evaporator area, and t is the irradiation time.

The evaporation efficiency (η) can be calculated by the following Equation 2.

$$\eta = \dot{m}\ h_{lv} / C_{opt} P_0 \quad (2)$$

Where $\dot{m}$ was the mass flux ($\dot{m} = m_{Light} - m_{Dark}$) (kg m^{-2} h^{-1}), C_{opt} is the multiple of 1 sun illumination density, P_0 is the solar intensity, and h_{lv} is the water evaporation enthalpy. According to the energy conversion principle, water evaporation rates can be expressed using the equations.

h_{lv} was calculated using Equations 3 and 4.

$$h_{lv} = C_p (T - T_0) + \lambda_{lv} \quad (3)$$

$$Uin = \nabla H_0\ m_0 = \nabla H_1\ m_1 \quad (4)$$

The energy input (Uin) in the darkness was equal. Among them, ∇H_0 (2444 J g^{-1}) and m_0 (0.098 kg·m^{-2}·h^{-1}) represent the enthalpy and rate of evaporation of bulk water in the dark, while ∇H_1 and m_1 (0.191 kg m^{-2} h^{-1}) represented the equivalent enthalpy of evaporation (λ_{lv}) and vaporization rate of BST/LFICS in the dark. C_p is the specific heat capacity of water (4.2 J g^{-1} K^{-1}), T_0 is the initial temperature of water, and T is the temperature of steam.

The following assumptions were made for all calculations:

1. Steady-state evaporation conditions were achieved during the test period.
2. Heat losses to the surrounding environment (convection, conduction, radiation) were corrected for via the dark evaporation baseline.
3. The effective enthalpy h_{lv} was constant for each sample during the test.
4. The incident solar intensity was uniform and stable at 1000 W·m^{-2} throughout the measurement.

A detailed example calculation for TiOC@SA-TiOC is now provided below, and all other samples follow the same stepwise calculation:

1. Net evaporation rate: $\dot{m} = 2.61 - 0.39 = 2.22$ kg·m^{-2}·h^{-1}
2. Effective enthalpy:

$h_{LV} = C_p (T - T_0) + \nabla H_0\ m_0/m_1 = 4.2*(373.0\text{-}303.5) + 0.19*2444/0.39 = 1493.87$ J·g^{-1}

3. Efficiency: $\eta = \dot{m}\ h_{lv} / C_{opt} P_0 = 2.22*1493.87/3600*100\% = 92.19\%$

2. Theoretical Simulation

Spin-polarized density functional theory (DFT) calculations were performed using the Vienna ab initio simulation package (VASP) with the projector augmented wave (PAW) method.[3,4] The Perdew–Burke–Ernzerhof (PBE) functional within the Dudarev +U scheme was used to describe the Ti 3*d* states, with U_{eff} = 4.0 eV.[5] Dispersion interactions were treated using the DFT-D3 method with Becke–Johnson damping. A plane-wave cutoff energy of 450 eV was employed.[6] Local bulk-like defect thermodynamics were modeled using a 2 × 2 × 1 supercell of anatase TiO_2, containing 16 Ti and 32 O atoms. The Brillouin zone was sampled using a 3 × 3 × 3 Monkhorst–Pack k-point mesh. The total-energy and force convergence criteria were set to 10^{-4} eV and 0.02 eV/Å, respectively. Three representative defect models were first considered: pristine anatase $(TiO_2)_{16}$, the intrinsic oxygen-vacancy model $(TiO_2)_{16}$-O_v, the isolated carbon-substituted model C-$(TiO_2)_{16}$, and the aromatic-carbon-associated model C_{10}/Csp^2-$(TiO_2)_{16}$.

The formation energies were calculated as follows:

$$E_f^{O_v} = E_{\left[(TiO_2)_{16}-O_v\right]} - E_{\left[(TiO_2)_{16}\right]} + \mu_O \quad (5)$$

$$E_f^{C@O_v} = E_{\left[C-(TiO_2)_{16}\right]} - E_{\left[(TiO_2)_{16}-O_v\right]} - \mu_C \quad (6)$$

$$E_f^{C_{10}/C_{sp^2}@3O_v} = E_{\left[C_{10}/C_{sp^2}-(TiO_2)_{16}\right]} - E_{\left[(TiO_2)_{16}-3O_v\right]} - E_{C_{10}/C_{sp^2}} \quad (7)$$

where E[*] denotes the total energy of the corresponding supercell, $E_{[(TiO2)16]}$, $E_{[(TiO2)16\text{-}OV]}$, $E_{[(TiO2)16\text{-}OV]}$, $E_{[C\text{-}(TiO2)16]}$, $E_{[(TiO2)16\text{-}3OV]}$, $E_{[C10/Csp2\text{-}(TiO2)16]}$ and $E_{C10/Csp2}$ are total energies of the corresponding structure, the μ_O and μ_C denote as the chemical potential of the oxygen and carbon, respectively.

It should be noted that this DFT model was used to compare the relative thermodynamic stability of local OV-containing defect motifs in bulk-like anatase TiO_2. It does not explicitly describe the polymeric Ti(**D100**)$_n$ precursor, mesoscale porosity, surface reconstruction, oxygen transport, or the decomposition kinetics of **D100** during calcination.

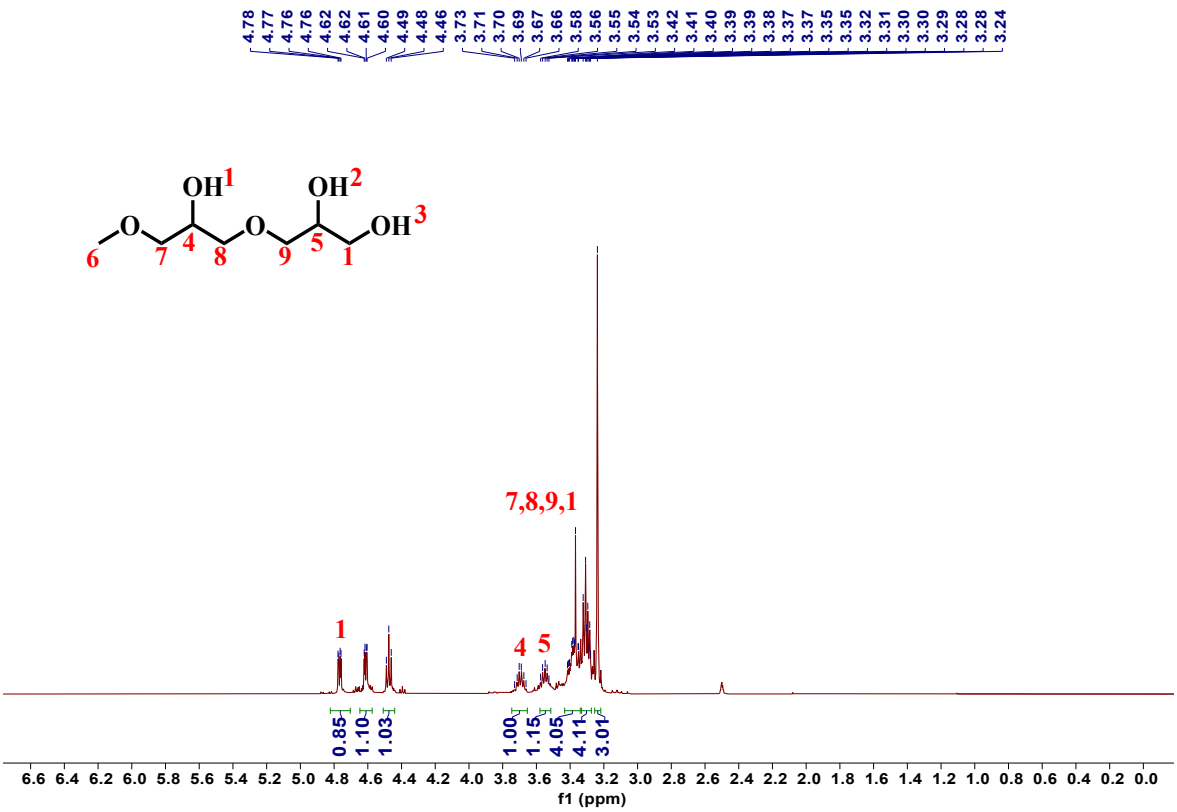

Fig. S1 [1]H NMR spectrum of **D100** in DMSO-d6 solution.

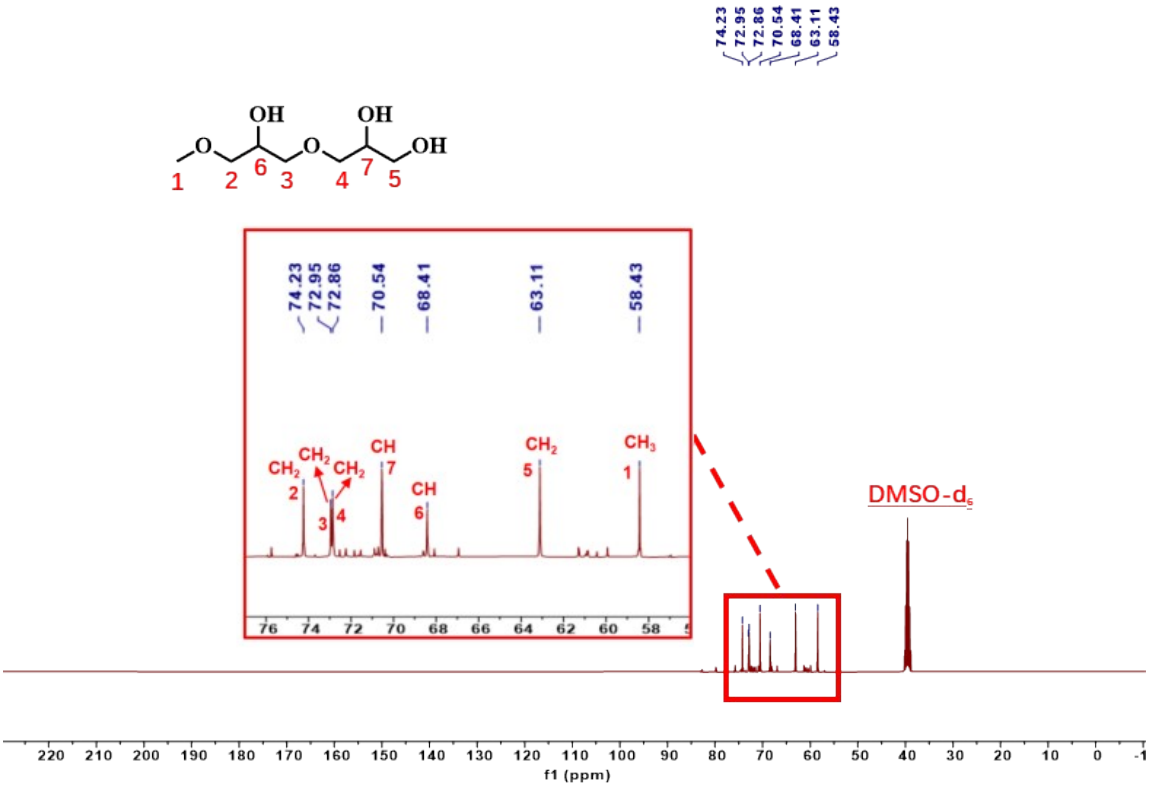

Fig. S2 [13]C NMR spectrum of **D100** in DMSO-d6 solution.

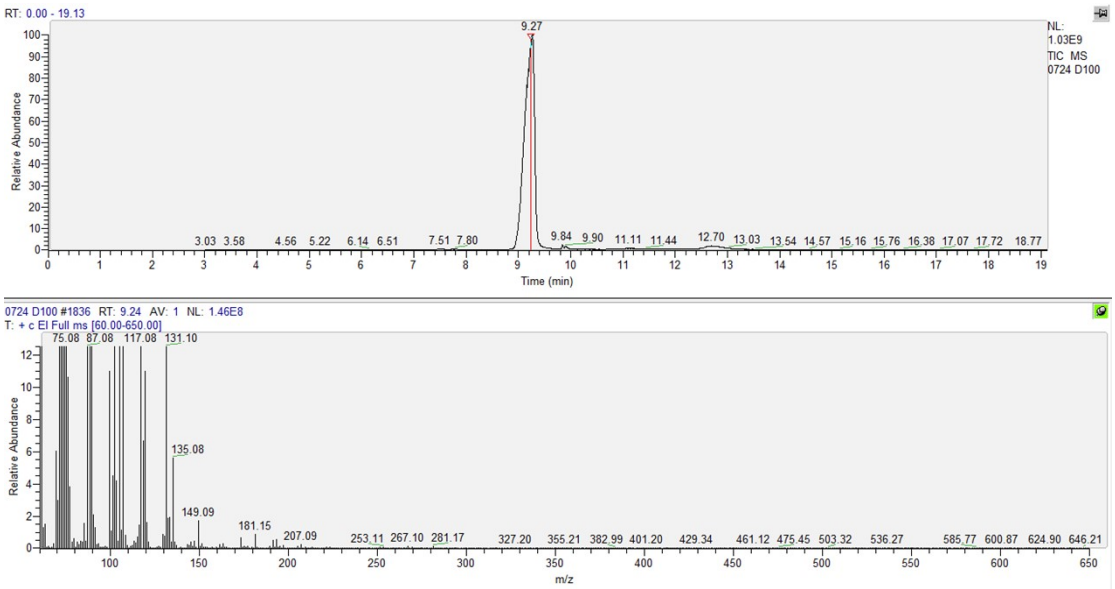

Fig.S3 GC-MS diagram of **D100**.

Fig. S4 Digital photo of hydrogel precursor Ti(**D100**)$_2$.

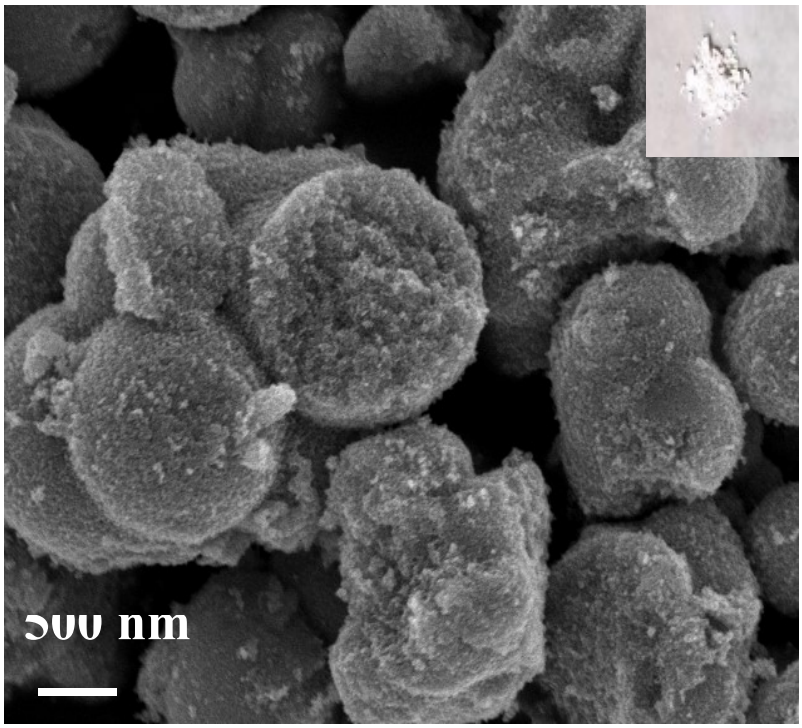

Fig. S5 FE-SEM image of TiOC-0 (inset: an optical image of the corresponding particles).

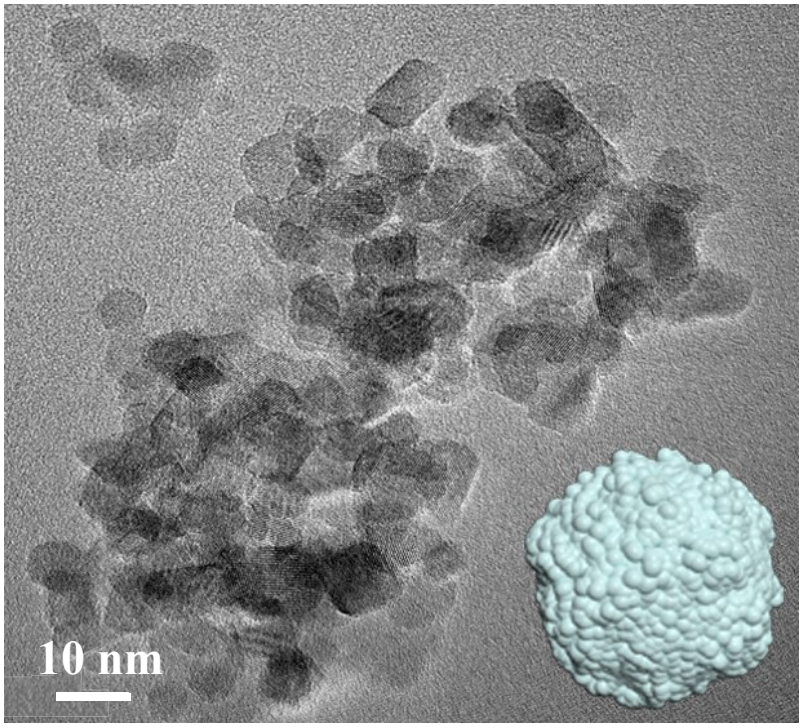

Fig. S6 TEM image of TiOC-0.

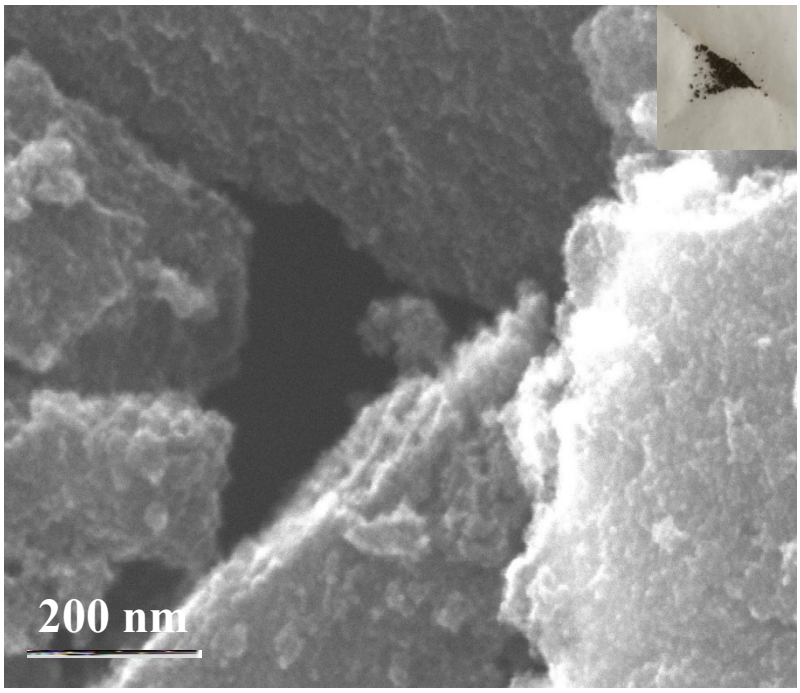

Fig. S7 FE-SEM images of TiOC-1 (inset: an optical image of the corresponding particles).

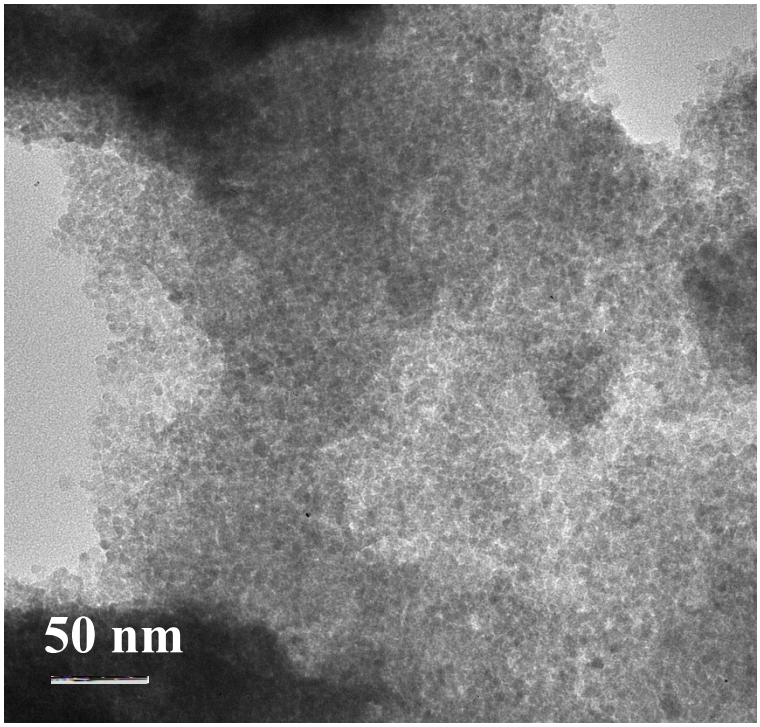

Fig. S8 TEM image of TiOC-1.

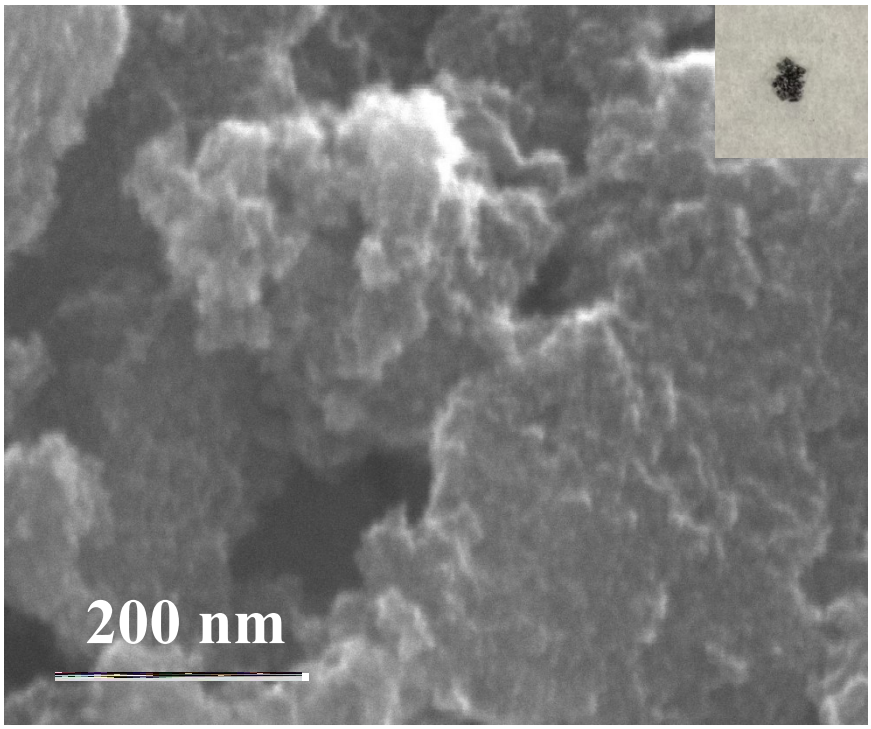

Fig. S9 FE-SEM image of TiOC-3 (inset: an optical image of the corresponding particles).

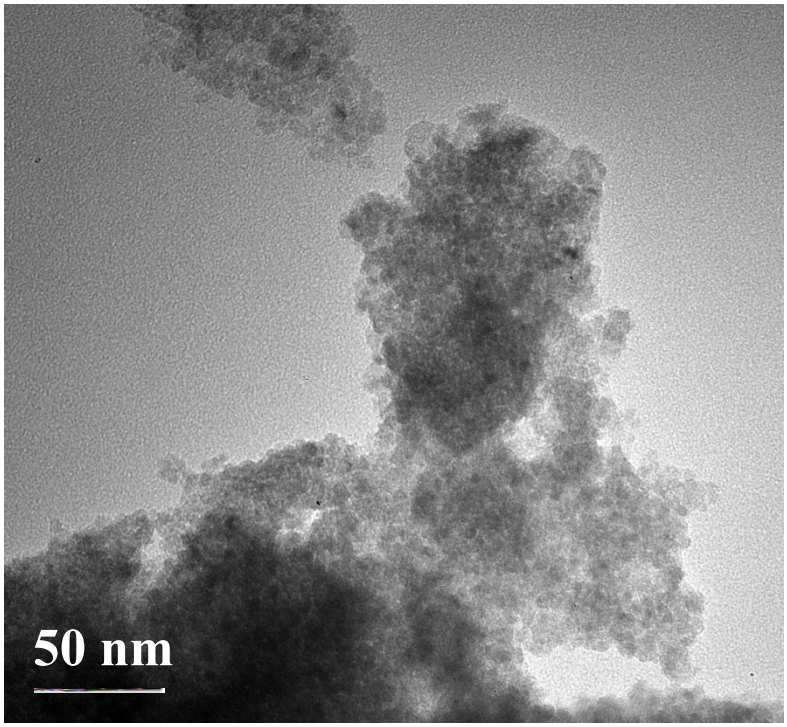

Fig. S10 TEM image of TiOC-3.

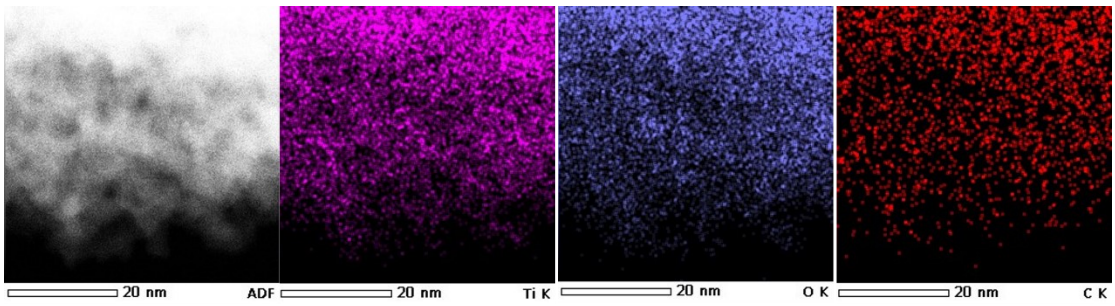

Fig. S11 HAADF-STEM image and element mappings of TiOC-2.

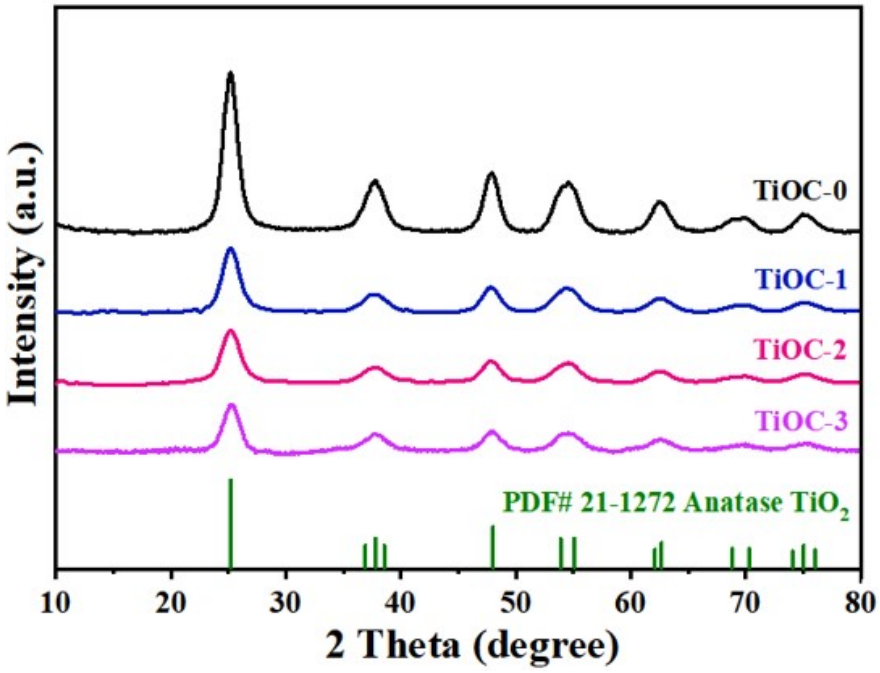

Fig. S12 XRD patterns of TiOC-n .

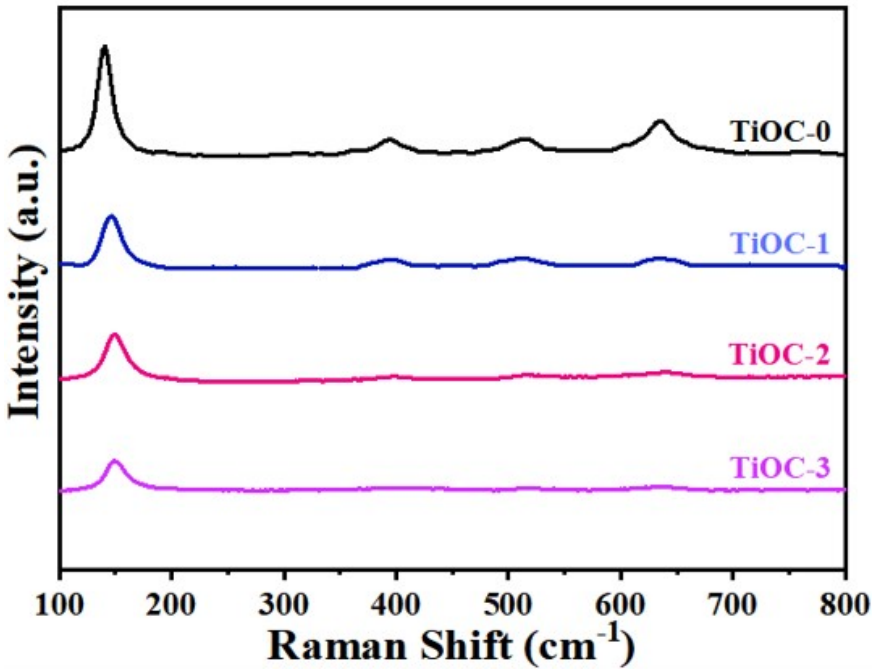

Fig. S13 Raman spectra of TiOC-n .

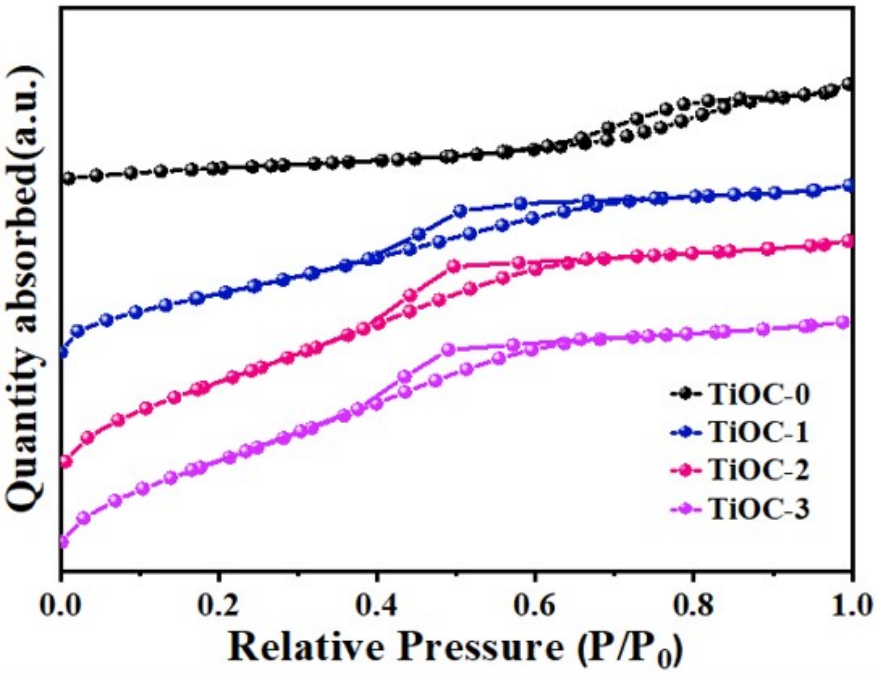

Fig. S14 N_2 adsorption-desorption isotherms of TiOC-n .

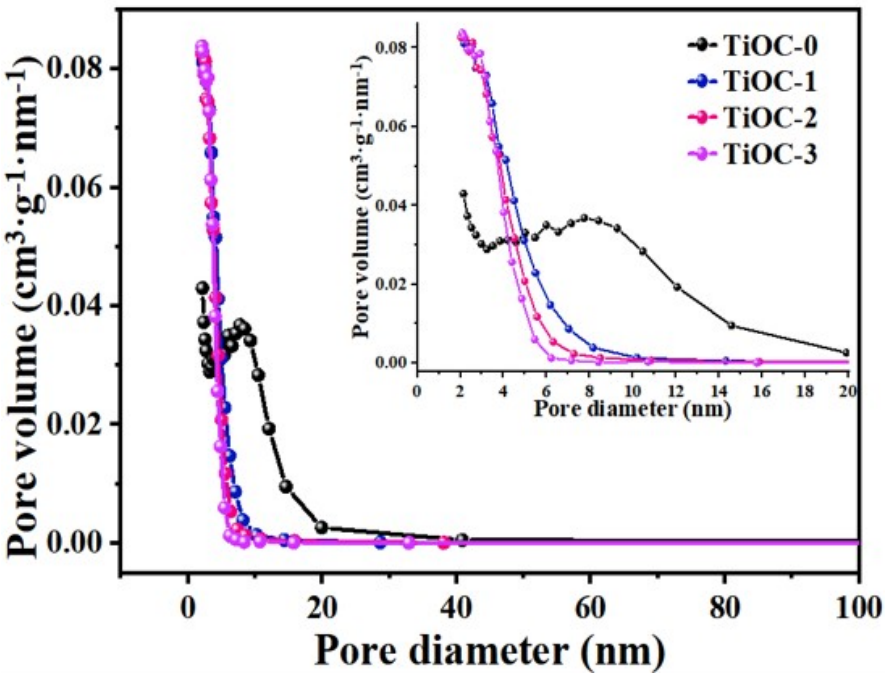

Fig. S15 Pore diameter distribution of TiOC-n .

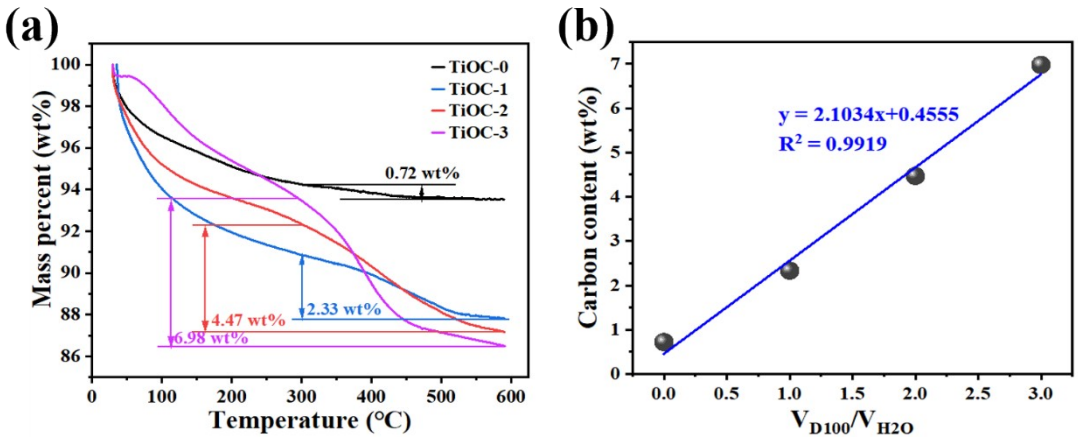

Fig. S16 (a) TG curves of various TiOC-n and (b) their fitting result based on TGA.

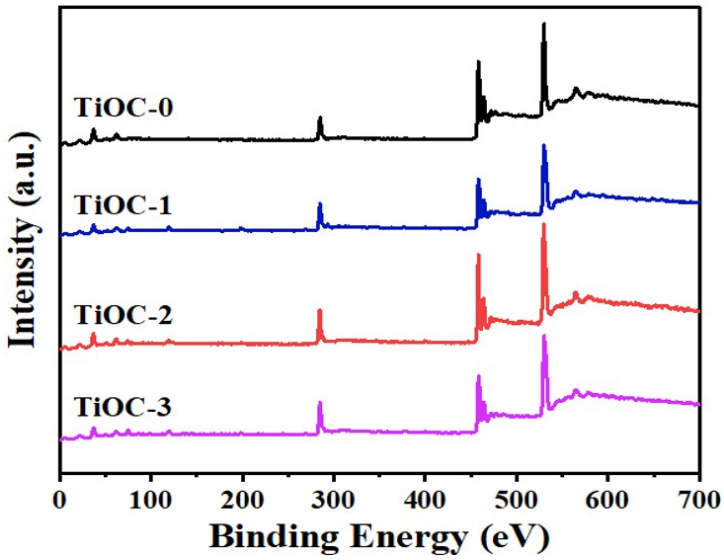

Fig. S17 XPS spectra of TiOC-n.

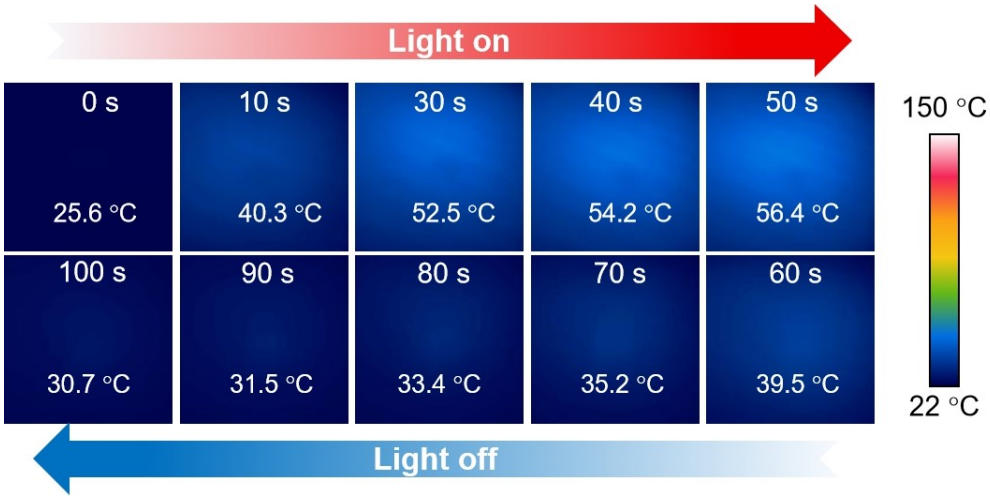

Fig. S18 IR camera images of TiOC-0 under on/off 4 kW m^{-2} illumination.

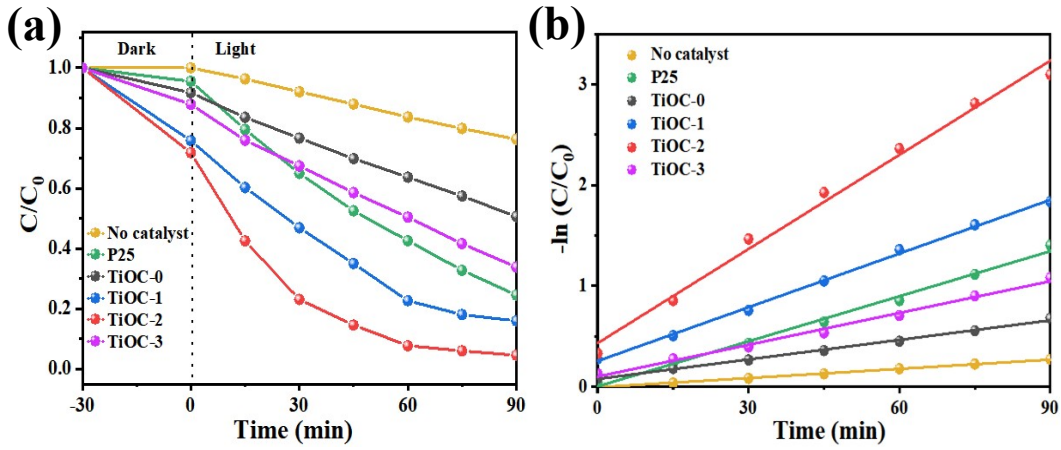

Fig. S19 Photocatalytic MB degradation performance of P25 and TiOC-n under 1 kW m^{-2} illumination.

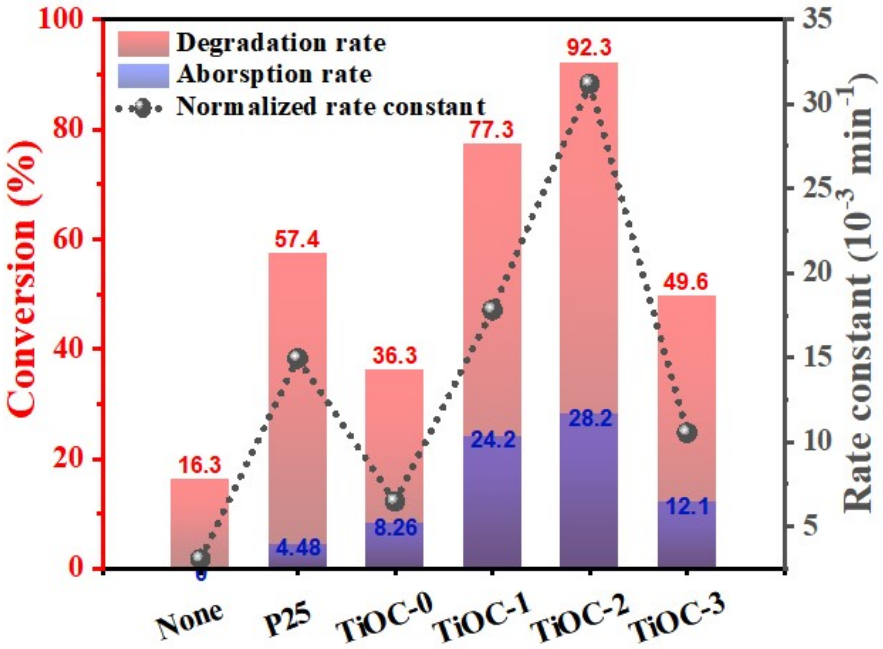

Fig. S20 Photocatalytic MB degradation performance of P25 and TiOC-n under 1 kW m^{-2} illumination.

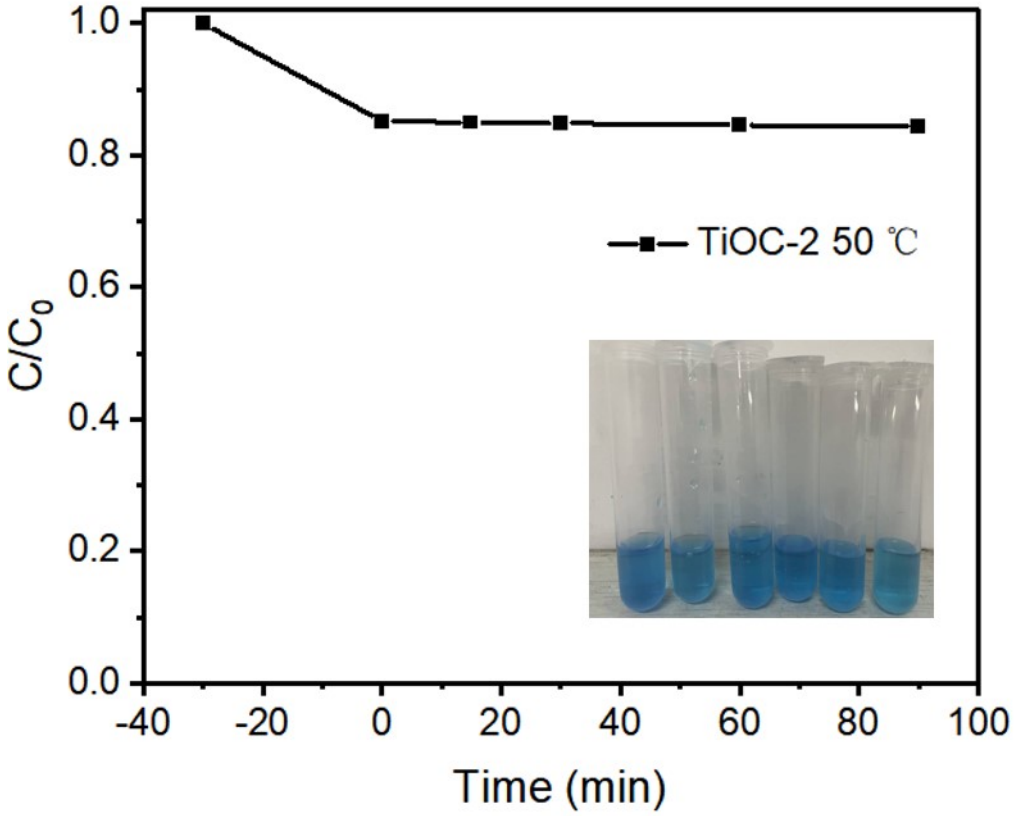

Fig. S21 MB degradation performance of TiOC-2 at 50 °C in dark.

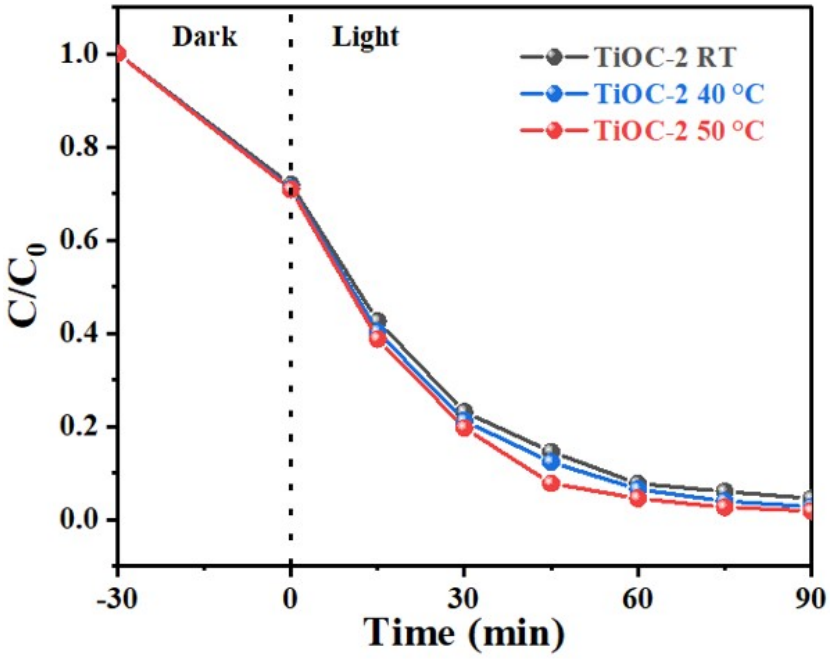

Fig. S22 Photocatalytic MB degradation performance of TiOC-2 at various temperature under 1 kW m^{-2} illumination.

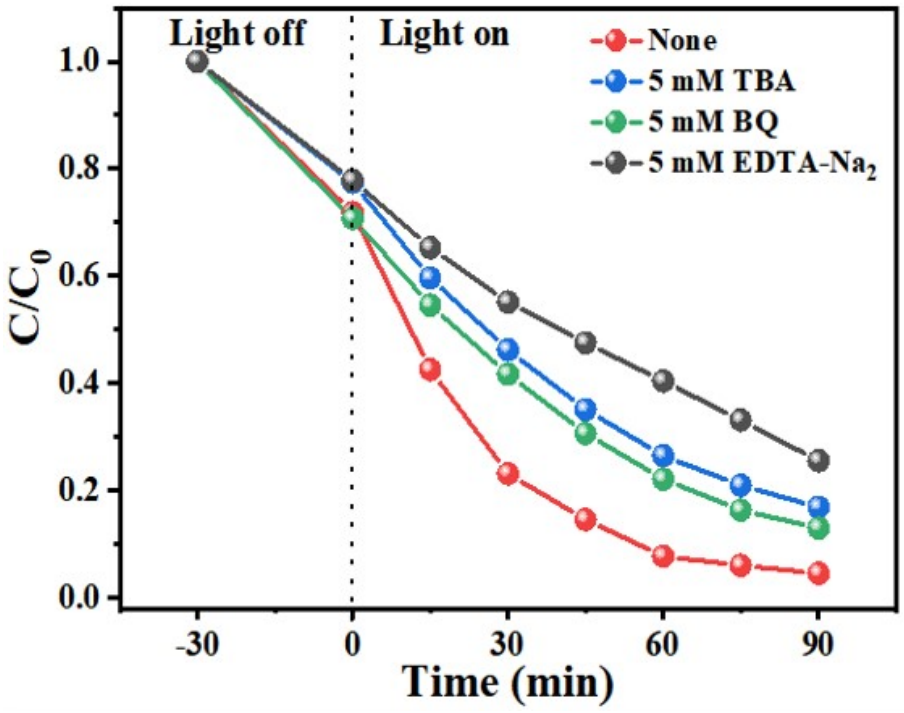

Fig. S23 The reactive specie scavenger experiments in MB photocatalytic degradation of TiOC-2 under 1 sun irradiation. The scavengers used were benzoquinone (BQ) for superoxide radicals ($\bullet O_2^-$), tert-butanol (TBA) for hydroxyl radicals (•OH), and EDTA-Na_2 for photogenerated holes (h^+), respectively.[7, 8]

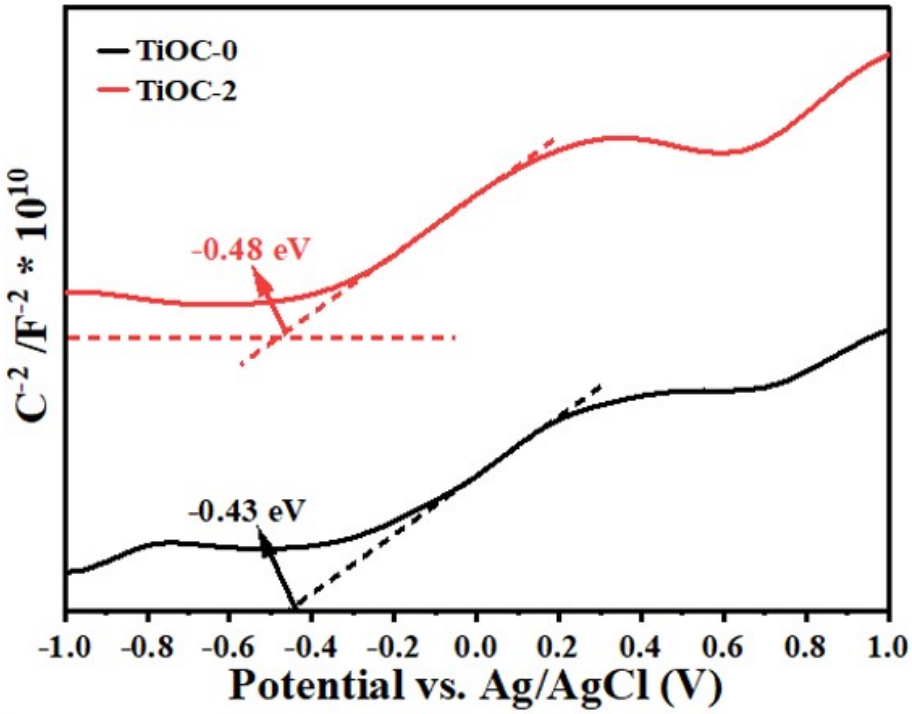

Fig. S24 Mott–Schottky diagrams of TiOC-0 and TiOC-2.

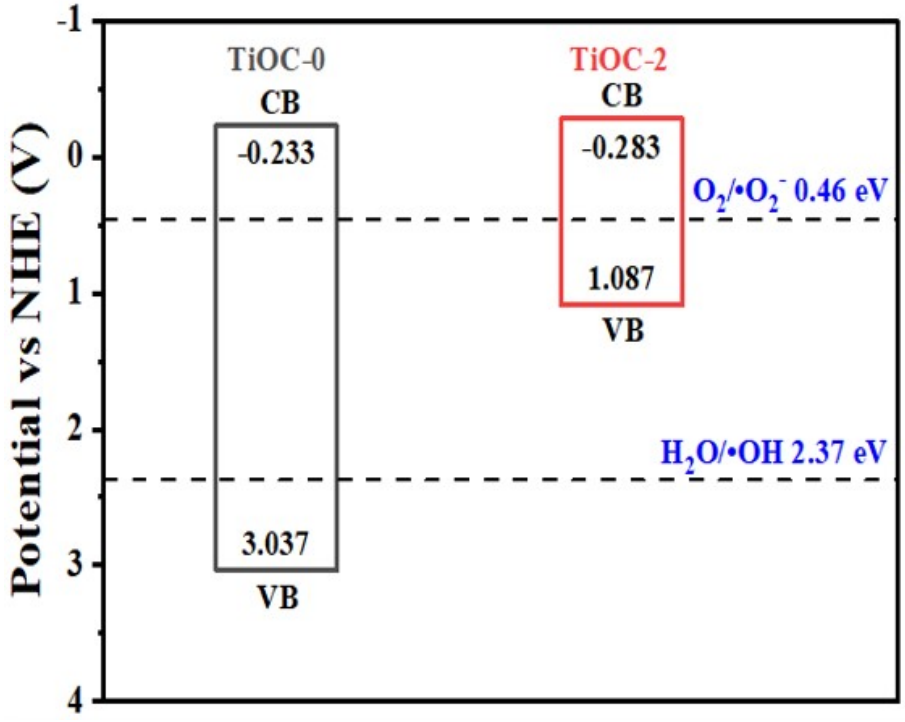

Fig. S25 Electronic band structures of TiOC-0 and TiOC-2. The flat-band potentials were determined vs. Ag/AgCl. The conduction band (E_{CB}) position was calculated vs. NHE according to the equation $E_{CB} = E_{(Ag/AgCl)} + 0.197$ V, the valence band (E_{VB}) position was calculated according to the equation $E_g = E_{VB} - E_{CB}$.[9,10]

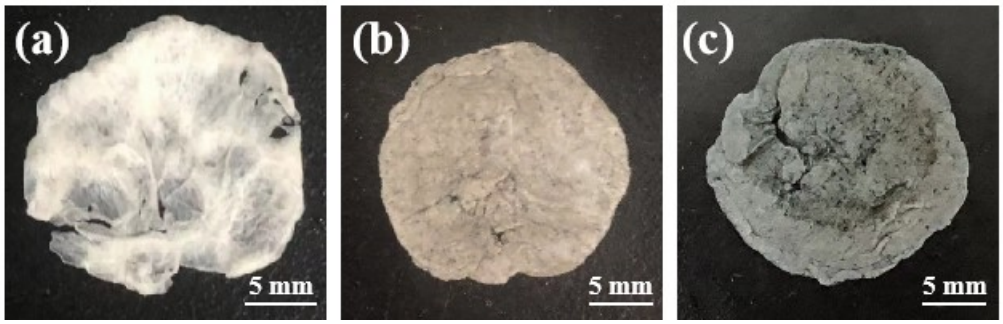

Fig. S26 Top digital photographs of as-prepared (a) SA, (b) SA-TiOC and (c) TiOC@SA-TiOC aerogels.

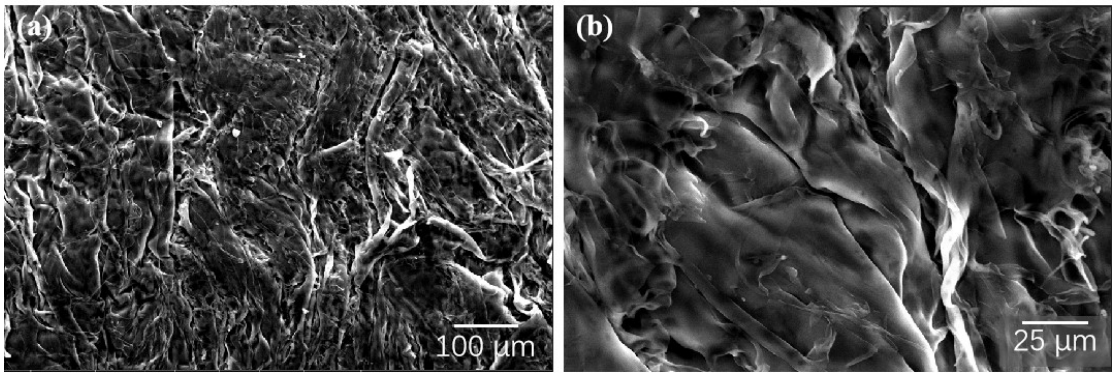

Fig. S27 FE-SEM image of SA aerogel.

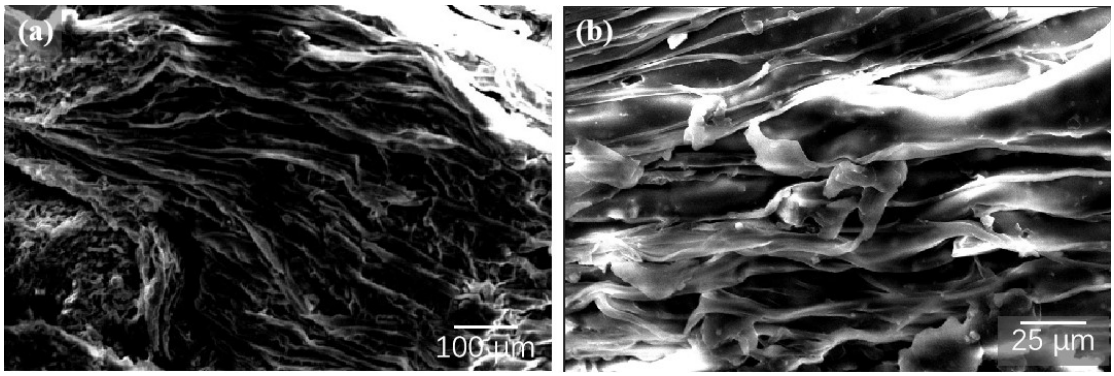

Fig. S28 FE-SEM image of SA-TiOC aerogel.

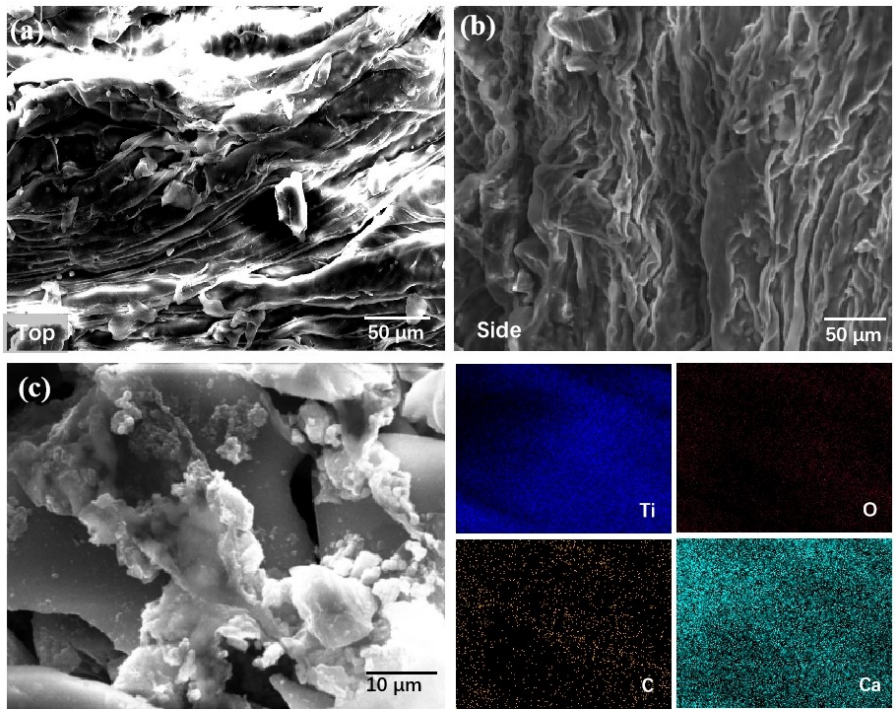

Fig. S29 FE-SEM image of TiOC@SA-TiOC aerogels (a) the top view image, (b) cross-sectional view, and (c) EDS mapping.

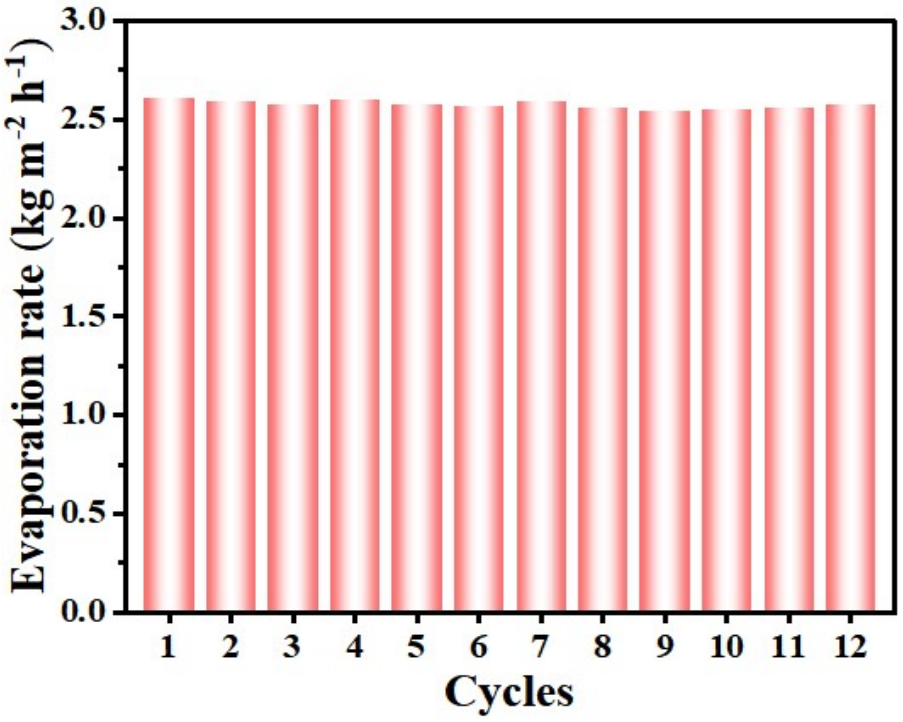

Fig. S30 Cycling stability of the TiOC@SA-TiOC evaporator.

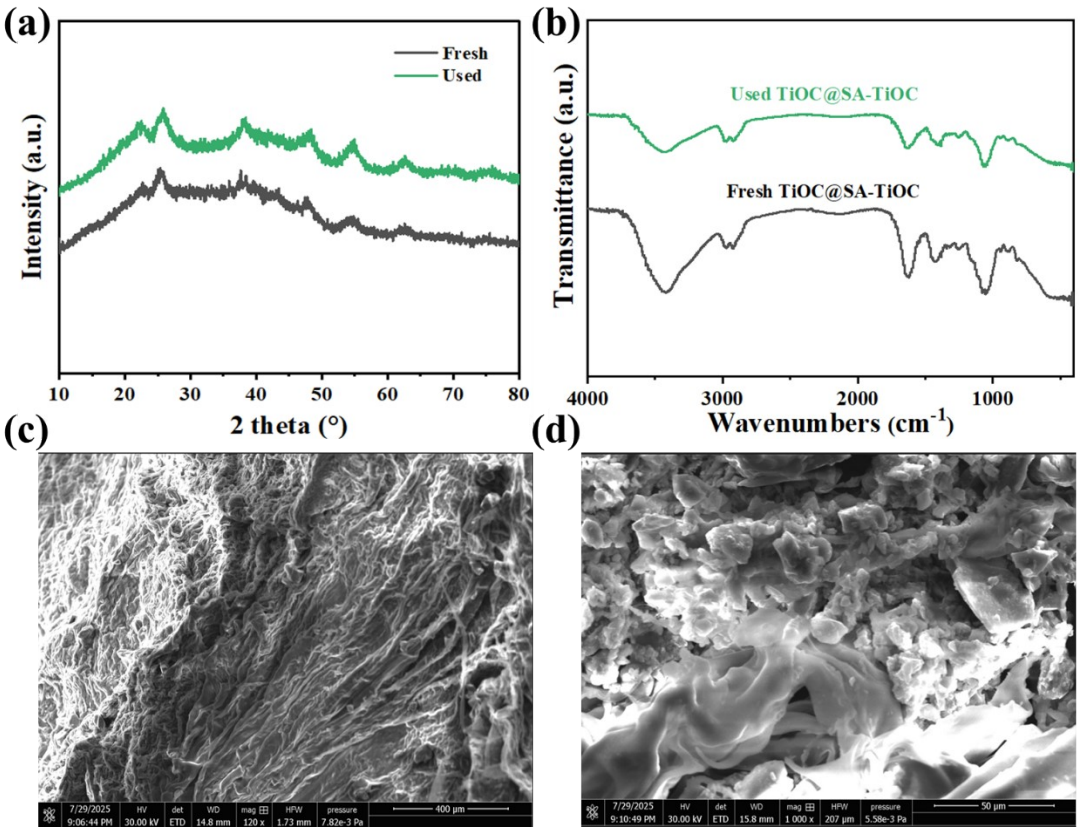

Fig. S31 Surface and morphology stability of the TiOC@SA-TiOC evaporator.（a）XRD patterns,（b）FTIR spectra, and（c,d）SEM after evaporation test.

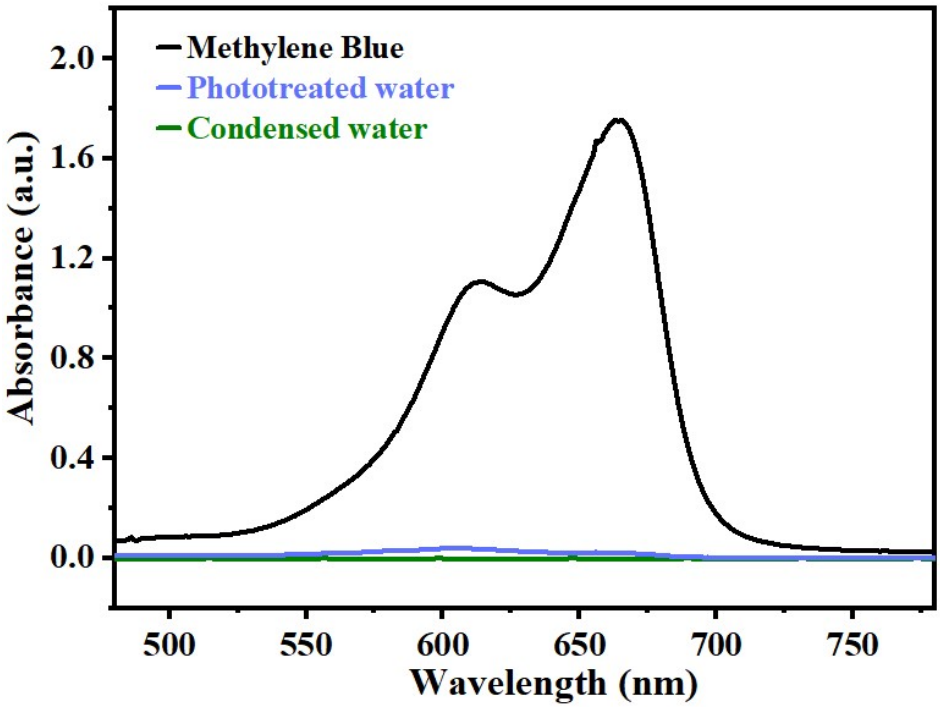

Fig. S32 TiOC@SA-TiOC evaporator for water samples taken during solar powered water

purification and MB degradation.

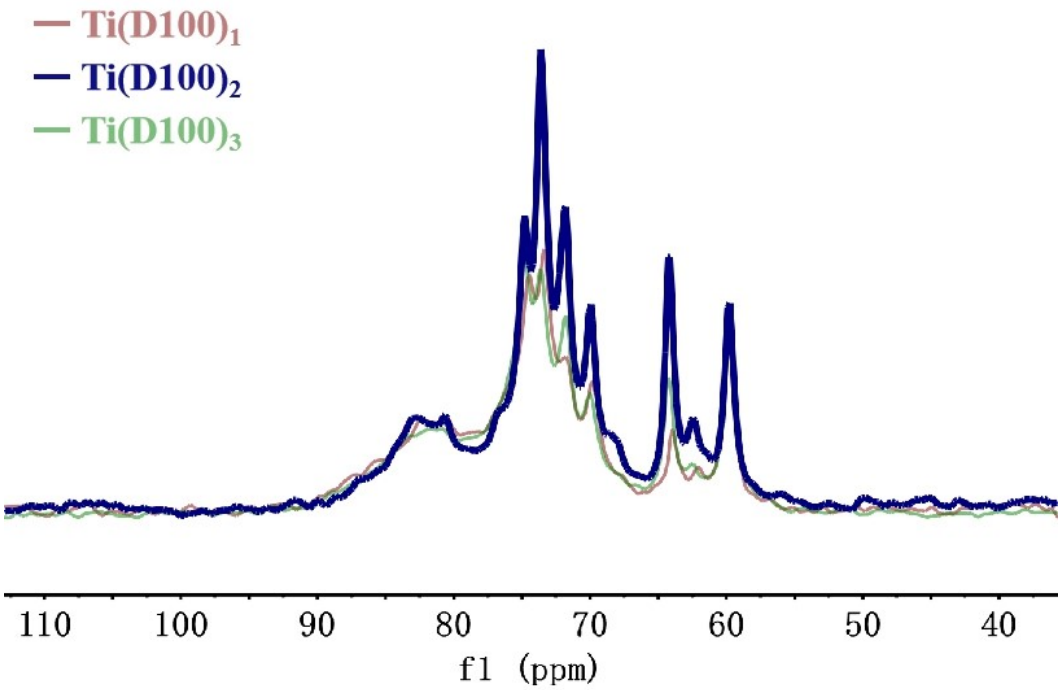

Fig. S33 Solid-state CP/MAS ^{13}C NMR spectra of Ti(**D100**)$_n$.

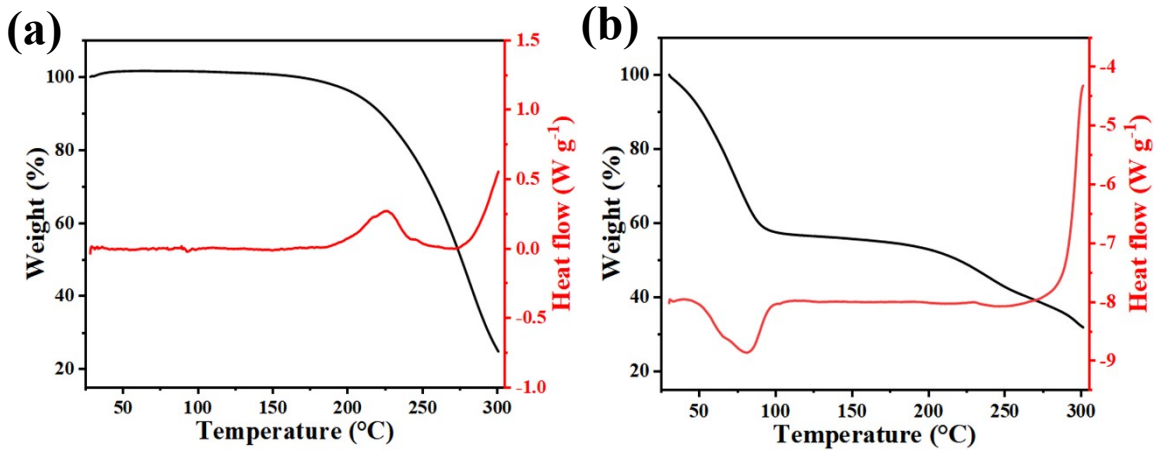

Fig. S34 The DTG-DSC curves of (a) **D100** and (b) Ti(**D100**)$_2$.

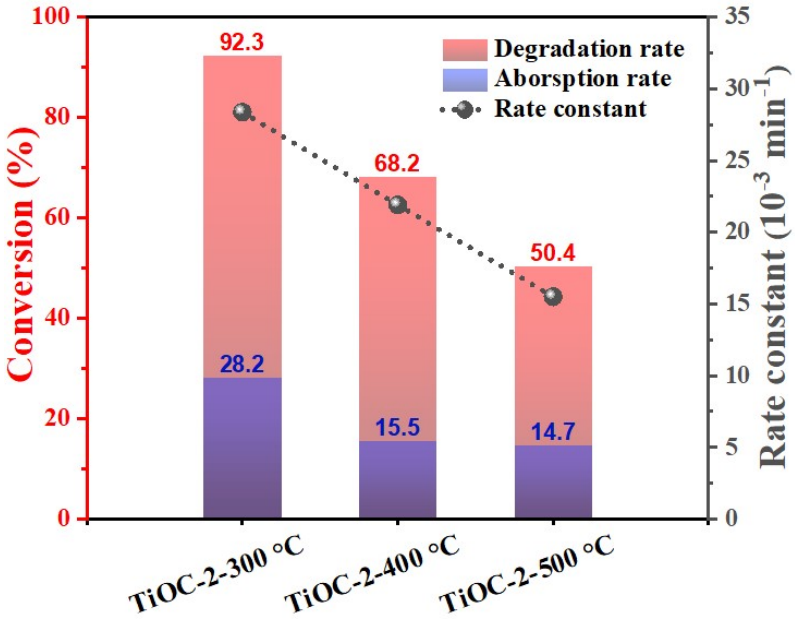

Fig. S35 Photocatalytic MB degradation performance of TiOC-2-300 °C, TiOC-2-400 °C and TiOC-2-500 °C.

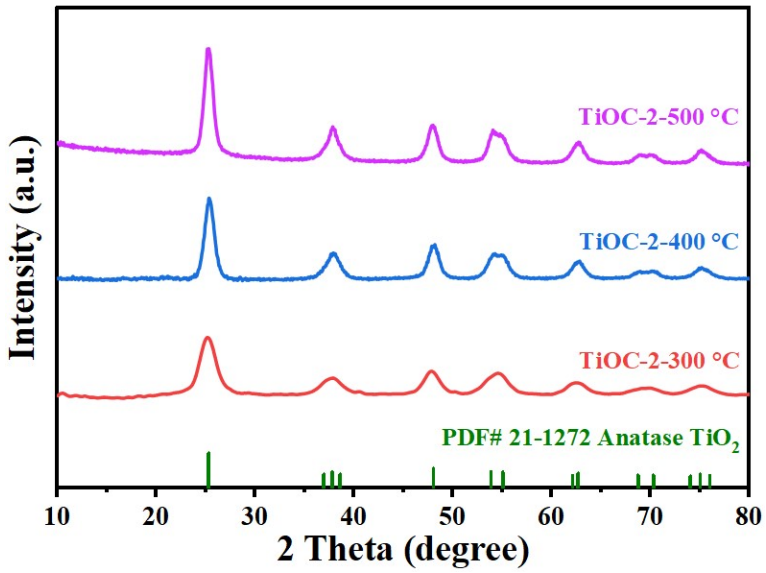

Fig. S36 XRD patterns of TiOC-2-300 °C, TiOC-2-400 °C and TiOC-2-500 °C.

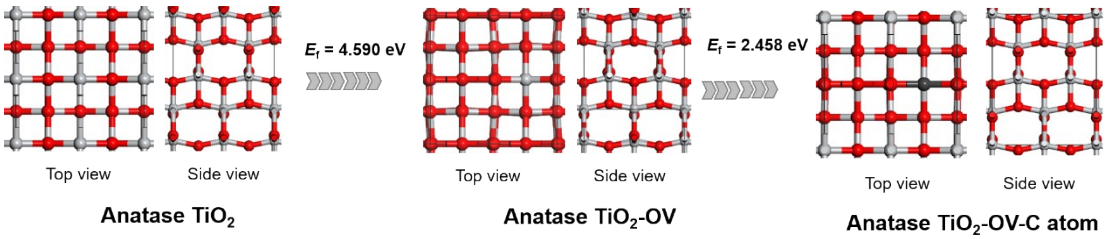

Fig. S37 Optimized local defect models used for DFT formation-energy calculations in bulk-like anatase TiO_2: pristine $(TiO_2)_{16}$, intrinsic OV $(TiO_2)_{16}$–O_v, isolated C-substituted model.

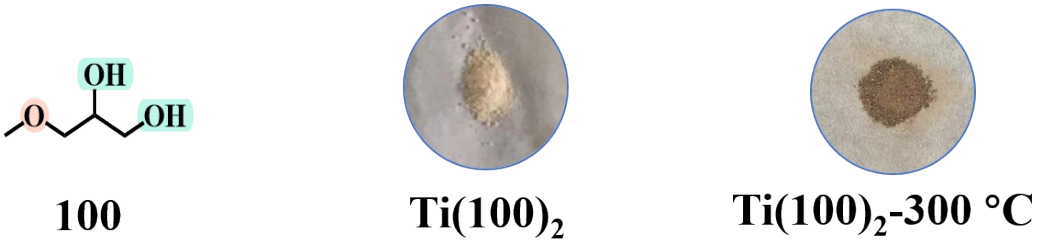

Fig. S38 Digital photographs of Ti(**100**)$_2$ and Ti(**100**)$_2$-300 ºC.

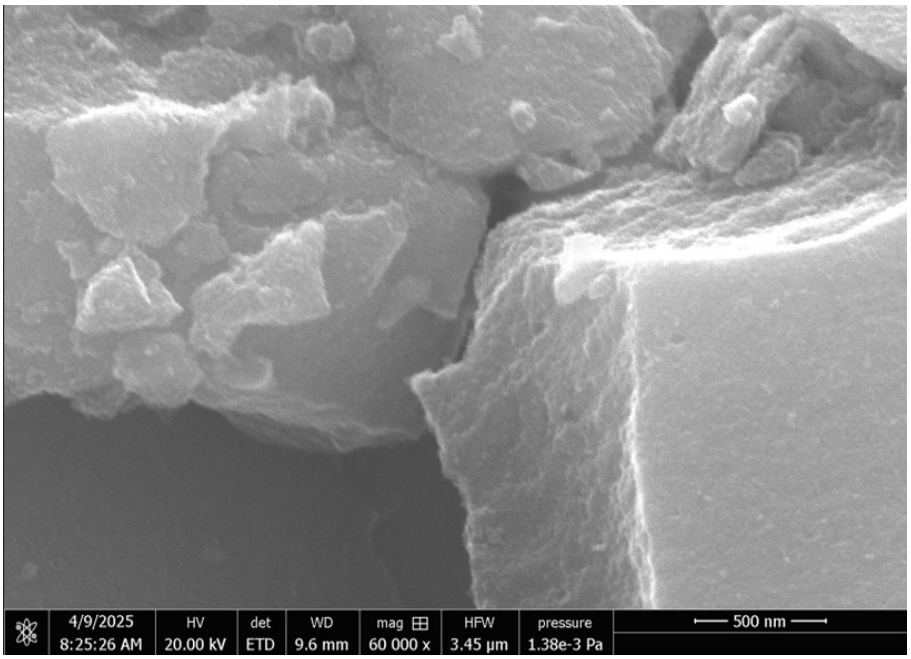

Fig. S39 FE-SEM image of Ti(**100**)$_2$-300 ºC.

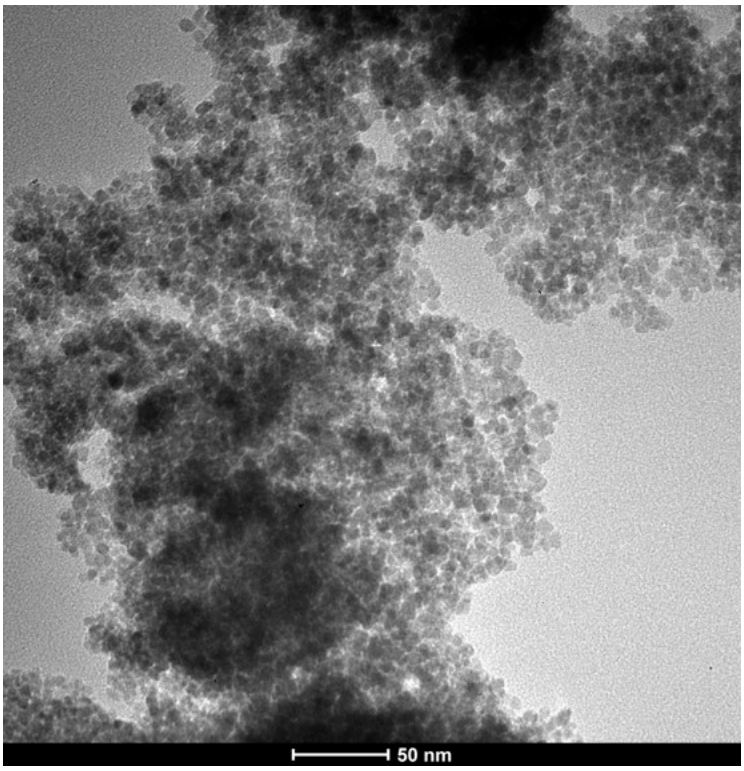

Fig. S40 TEM image of Ti(**100**)$_2$-300 ºC.

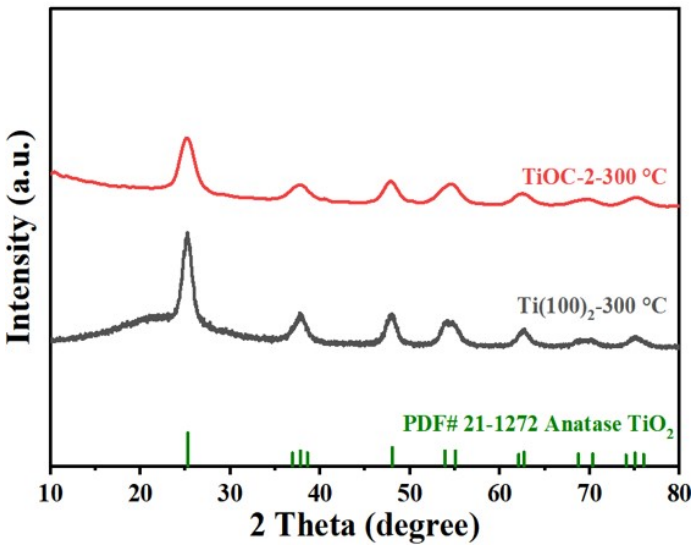

Fig. S41 XRD patterns of TiOC-2-300 °C and Ti(**100**)$_2$-300 ºC.

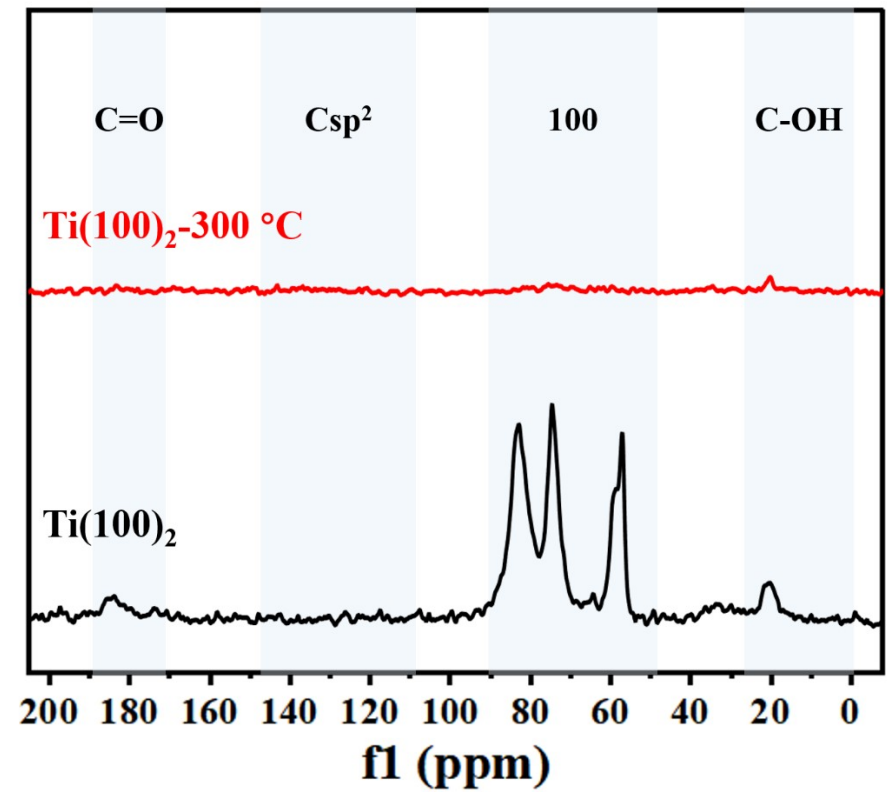

Fig. S42 Solid-state CP/MAS ^{13}C NMR spectra of Ti(**100**)$_2$ and Ti(**100**)$_2$-300 ºC.

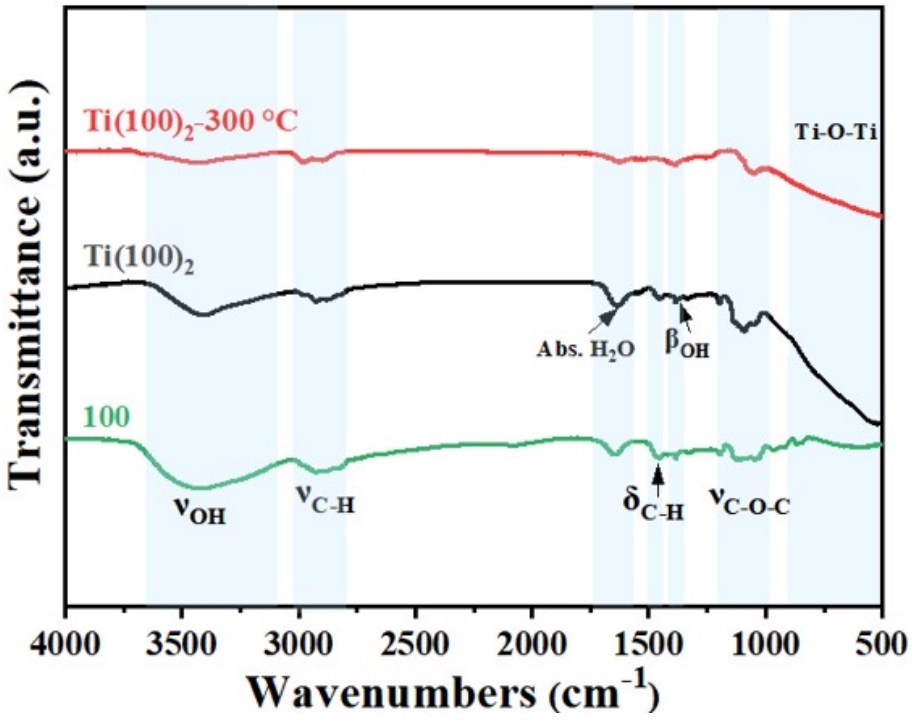

Fig. S43 FTIR spectra of **100**, Ti(**100**)$_2$ and Ti(**100**)$_2$-300 ºC.

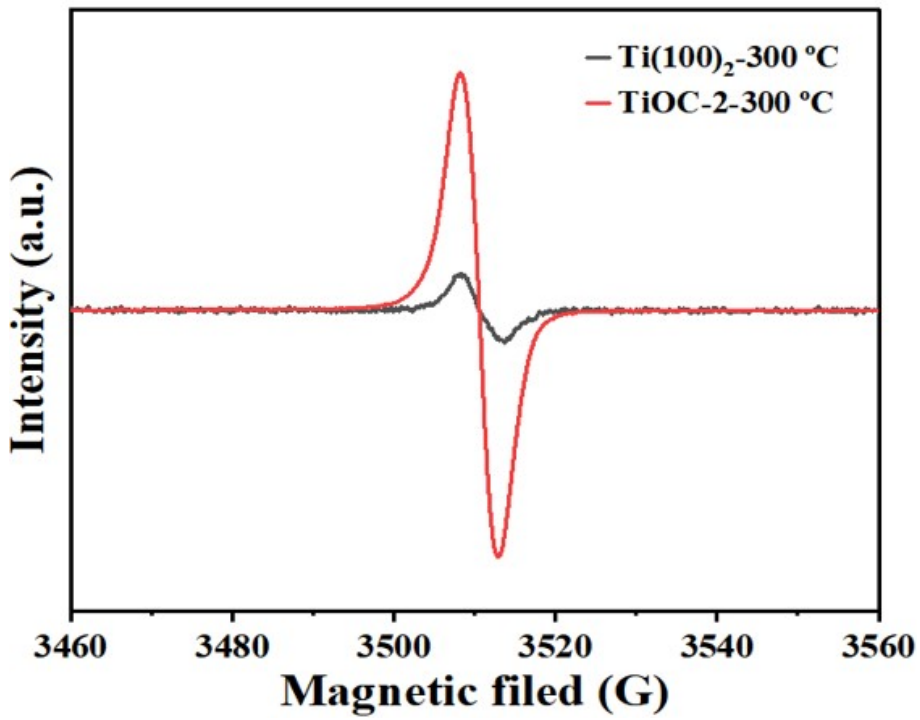

Fig. S44 EPR spectra of Ti(**100**)$_2$-300 ºC and TiOC-2-300 °C.

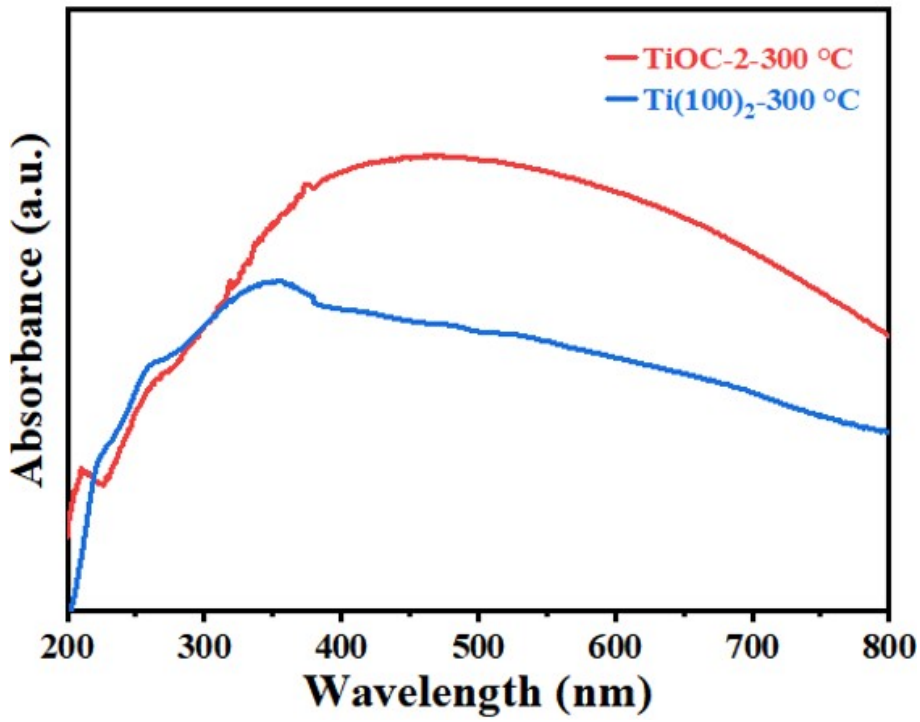

Fig. S45 UV–vis-NIR DRS absorption spectra of Ti(**100**)$_2$-300 ºC and TiOC-2-300 °C.

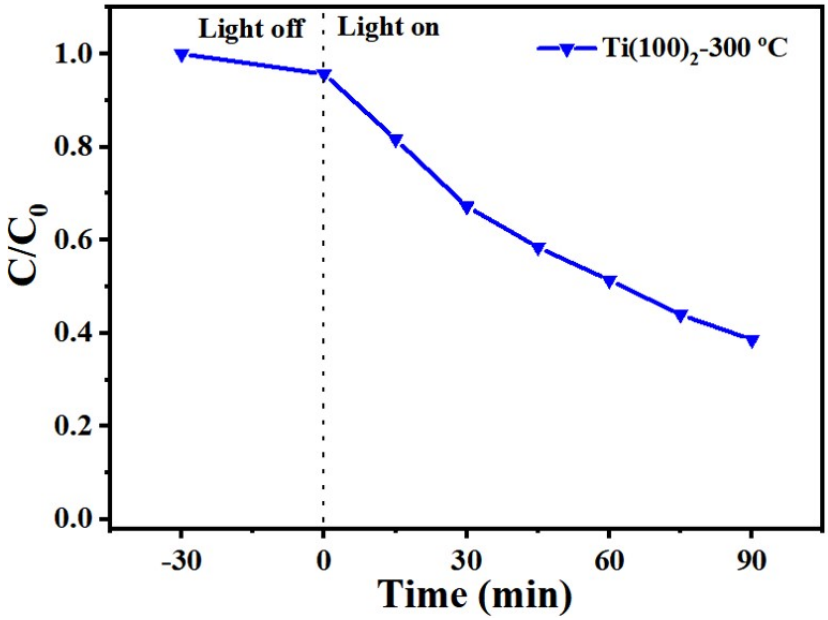

Fig. S46 Photocatalytic MB degradation performance of Ti(**100**)$_2$-300 ºC.

Table S1 BET and surface area-normalized rate constant results

Sample	A_S	Average pore volume	Average pore diameter	k_a
	$m^2 g^{-1}$	$cm^3 g^{-1}$	nm	$*10^{-5}$ g $m^{-2}min^{-1}$
TiOC-0	179.04	0.45	6.67	4.40
TiOC-1	263.21	0.25	3.52	6.48
TiOC-2	267.31	0.21	3.29	10.61
TiOC-3	258.47	0.19	3.15	5.05

Table S2. Intensity ratio calculated from high-resolution XPS spectra.

	O_{latt}	O_{ads}	O-H_2O	$O_{ads}/(O_{latt}$+O-$H_2O)$	Ti^{3+}/ Ti^{4+}
TiOC-0	82.3%	13.9%	3.8%	16.1%	0
TiOC-1	61.3%	28.2%	10.5%	39.3%	20.8
TiOC-2	54.9%	34.5%	10.6%	52.7%	35.0
TiOC-3	56.8%	32.3%	10.9%	47.7%	24.4

Table S3 Calculated TPRL parameters of TiOC.

Samples	τ_1 (ns) [a]	τ_2 (ns) [a]	I_1 (%)[b]	I_2 (%)[b]	I_1/ I_2
TiOC-0	0.925±0.023	6.536±0.103	19.85	80.15	0.25
TiOC-1	1.278±0.039	7.286±0.132	18.15	81.82	0.22
TiOC-2	1.633±0.042	6.775±0.171	36.11	63.89	0.57
TiOC-3	1.170±0.079	4.690±0.317	31.67	68.33	0.46

[a] Two distinct lifetime components τ_1 and τ_2 calculated by a biexponential function of time (t),

$$F(t) = A_1 e^{-\frac{1}{\tau_1}} + A_2 e^{-\frac{1}{\tau_2}} + y_0.$$

[b] The relative intensities of different lifetime components.

Table S4 Comparison of TiO_2 based solar evaporators under 1 sun simulated light.

Evaporators	Evaporation rate (kg m^{-2} h^{-1})	Energy efficiency (%)	C_{MB} (ppm)	Time (h)	Photocatalytic performance (%)	Ref.
Defective Black TiO_2 film[1]	1.624	85	-	-	-	11
Black TiO_2 nanocages film[1]	1.13	70.9	-	-	-	12
CDs/TiO_2 nanotube@Ti[1]	1.762	55.3	-	-	-	13
b-TiO_2/mesh[2]	0.92	-	-	-	-	14
Oxygen-deficient TiO_2 ceramics[2]	2.38	81.26	-	-	-	15
Black TiO_2/PVA[2]	2.492	-	-	-	-	16
PAM/SA/TiO_2-CQDs/CNTs 3D[2]	2.56	-	-	2	85.5	17
TiO_2/SiO_2@CNMs[2]	1.71	92.1	10	1.5	91.3	18
CNTs/TiO_2/Ag SWDIES[2]	1.46	-	10	4	87	19
TiO_2@CB/CF[2]	1.42	90.4	5	2	57	20
TiOC@SA-TiOC[2]	2.61	92.19	10	3	**91.2**	**This work**

[1] Calculate the photothermal efficiency according to formula $\eta = \dot{m}\cdot He/Qs$, where He is fixed at the bulk water phase-change enthalpy (2256–2260 J g^{-1}). This overestimates h_{lv} and results in artificially high efficiency values.

[2] Calculate the photothermal efficiency according to formula $\eta = \dot{m}\, h_{lv} / C_{opt} P_{0,}$ where h_{lv} is calibrated to match the system's actual evaporation enthalpy, producing efficiency values that reflect the real photothermal performance of the reactor.

Table S5. Intensity ratio calculated from high-resolution *in-situ* XPS spectra.

	O_{latt}	O_{ads}	O-H_2O	$O_{ads}/(O_{latt}+O\text{-}H_2O)$	Ti^{3+}/ Ti^{4+}
TiOC-2/300 ℃-1 h	70.6	15.8	13.6	18.8	44.9
TiOC-2/300 ℃-2 h	72.8	21.1	6.1	26.8	35.6
TiOC-2/400 ℃-1 h	85.5	9.8	4.7	10.9	8.1
TiOC-2/500 ℃-1 h	77.0	9.3	12.8	10.2	0

Table S6 Formation energy (E_f) for each optimized local defect models as a function of total energy of pristine $(TiO_2)_{16}$, intrinsic OV $(TiO_2)_{16}$–O_v, isolated C-substituted model, and aromatic Csp^2-associated OV-containing model.

Structure	**Energy (eV)**			
TiO_2 -Ov	$E_{[(TiO_2)_{16}]}$	μ_O	$E_{[(TiO_2)_{16}-O_v]}$	$E_f^{O_v}$
	-397.453	-4.930	-387.933	4.590
TiO_2 -C	$E_{[(TiO_2)_{16}-O_v]}$	μ_C	$E_{[C-(TiO_2)_{16}]}$	$E_f^{C@O_v}$
	-387.933	-8.390	-393.865	2.458
TiO_2 -3Ov-C_{10}/Csp^2	$E_{[(TiO_2)_{16}-3O_v]}$	$E_{C_{10}/C_{sp^2}}$	$E_{[C_{10}/C_{sp^2}-(TiO_2)_{16}]}$	$E_f^{C_{10}/C_{sp^2}@3O_v}$
	-367.815	-75.326	-445.967	-2.826

References

1 T. Zhang, Y. Lv, P. Cao, Z. Song, Q. Wang, Y. Guo, L. Hong, Y. Chen, Vine utilization strategy: biomass-based aerogel with vertically aligned channels for highly efficient interfacial solar evaporation. *Chem. Eng. J.*, 2025, **515**, 163828.

2 J.-W. Wang, X. Bao, M. Yuan, C. Zhu, L. Zhu, Chen, S. Easy access to robust rigid SiO_2-based photothermal aerogel for enhanced solar interfacial evaporation. *Sep. Purif. Technol.*, 2025, **353**, 128324.

3 G. Kresse, J. Furthmüller, Efficient iterative schemes for *ab initio* total-energy calculations using a plane-wave basis set. *Phys. Rev. B*, 1996, 11169-11186.

4 I. I. Solovyev, P. H. Dederichs, V. V. Anisimov, Corrected atomic limit in the local-density approximation and the electronic structure of d impurities in Rb. *Phys. Rev. B*, 1994, **50**, 16861-16871.

5 J.K. Nørskov, J. Rossmeisl, A. Logadottir, Origin of the overpotential for oxygen reduction at a fuel-cell cathode. *J. Phys. Chem. B*, 2004, **108**, 17886-17892.

6 S. Grimme, J. Antony, S. Ehrlich, H. Krieg, A consistent and accurate ab initio parametrization of density functional dispersion correction (DFT-D) for the 94 elements H-Pu. *J. Chem. Phys.*, 2010, **132**, 154104.

7 S.Cong, J. Cai, X. Li, J. You, L. Wang, X. Wang, Direct Z-scheme xylan-based carbon dots@TiO_{2-x} nanocomposites for visible light driven photocatalytic of dye degradation and antibacterial. *Adv. Funct. Mater.*, 2024, 2401540.

8 S. Yan, Y. Li, F. Xie, J. Wu, X. Jia, J. Yang, H. Song, Z. Zhang, Environmentally safe and porous MS@TiO_2@PPy monoliths with superior visible-light photocatalytic properties for rapid oil-water separation and water purification. *ACS Sustainable Chem. Eng.*, 2020, **8**, 5347-5359.

9 B. Shen, Y. Xia, Y. Zhou, J.Wang, Y. Feng, W. Xu, Synthesis of highly-ordered ternary CeO_2-AuNR-Cu_2O Janus structure with dual Schottky junctions for highly efficient photocatalysis. *Sci. China Mater.*, 2025, **68**, 1906-1917.

10 M. Zhao, X. Wang, M. Gao, J. Zhang, Y. Lu, Y. Guo, L. Hu, X. Su, J. Feng, Co^{3+} in cobalt (100)/g-C_3N_4 facilitating the conversion of superoxide radicals into hydroxyl radicals and improving photocatalysis. *Appl. Surf. Sci.*, 2025, **706**, 163536.

11 P. Zheng, J. Tang, Z. Zhou, L. Gong, H. Yang, X. Jia, X. Li, Y. Liu, L. Tan, Ultrafast Synthesis of Defective Black TiO_2 via One-Step NaN_3 Deflagration for High-efficiency Solar Water Evaporation, *Surf. Interfaces*, 2021, **22**, 100901.

12 G. Zhu, J. Xu, W. Zhao, F. Huang, Constructing Black Titania with Unique Nanocage Structure for Solar Desalination, *ACS Appl. Mater. Interfaces*, 2016, **8**, 31716-31721.

13 C. Xue, D. Li, Y. Li, N. Li, F. Zhang, Y. Wang, Q. Chang, S. Hu, 3D-carbon dots decorated black TiO_2 nanotube Array@Ti foam with enhanced photothermal and photocatalytic activities, *Ceram. Int.*, 2019, **45**, 17512-17520.

14 S. Zhu, Z. Yu, L. Zhang, S. Watanabe, Solution Plasma-Synthesized Black TiO_2 Nanoparticles

for Solar–Thermal Water Evaporation, *ACS Appl. Nano Mater.*, 2021, **4**, 3940-3948.

15 L. Chen, D. Yao, M. Zhu, J. Zhao, Y. Xia, Y.-P. Zeng, Gradient structure oxygen-deficient TiO_2 ceramics for interfacial evaporation by direct ink writing, *Ceram. Int.*, 2025, **51**, 34127-34133.

16 X. Zhang, Y. Cui, C. Wang, Oxygen Vacancy-Engineered Black TiO_2/PVA Hydrogel for High-Efficiency Solar-Driven Interfacial Evaporation, *Processes*, 2026, **14**, 1159.

17 G. Liu, Q. Ma, Z. Li, J. Zhang, K. Lei, D. Li, M. Xue, W. Wu, J. Du, X. Zhang, Dual-functional hydrogel evaporator with CQDs loaded TiO_2 and CNTs for efficient eutrophic water body purification, *Desalination*, 2026, 622, 119752.

18 W. Wang, Y. Chen, N. Wang, M. Jensen, X. Li, Facile preparation of anatase coated nanofiber mats for multifaceted water treatment, *Chem. Eng. J.*, 2024, **485**, 149764.

19 X. Sun, Q. Ye, Y. Xia, X. Ji, Q. Cai, Z. Hu, S. Rao, X. Wu, An easily scalable multi-unit solar/wave-driven interfacial evaporation system connected by a hinge-like structure for co-producing of fresh water and electricity, *Energ. Convers. Manage*, 2024, **322**, 119189.

20 Y. Tian, X. Yang, L. Xu, X. Wang, J. Yu, D. Wu, F. Li, T. Gao, A composite fabric with dual functions for high-performance water purification, *Materials*, 2022, **15**, 5917.